Nanoscale

PAPER

View Article Online
View Journal | View Issue

Cite this: *Nanoscale*, 2025, **17**, 27585

Boosting magnetoresistance in manganese phosphide helimagnets through iron oxide interface strain engineering

Nivarthana W. Y. A. Y. Mudiyanselage, *[a] Derick DeTellem,[a] Yasinthara M. Wadumesthri,[a] Amit Chanda,[b] Anh Tuan Duong, [c] Emmanuel Olawale,[a] Humberto Rodriguez Gutierrez, [a] Xiaomei Jiang,[a] Sarath Witanachchi[a] and Manh-Huong Phan *[a,d]

Helimagnetic materials exhibit complex non-collinear spin structures, making them promising candidates for next-generation magnetoresistive devices. Their unique magnetic textures can yield enhanced magnetoresistance effects compared to conventional materials, potentially improving the performance of magnetic sensors and memory technologies. In this study, an interface engineering strategy is presented that leverages strain induced by the structural phase transition of Fe_3O_4 to enhance the magnetoresistance (MR) effect in nanostructured manganese phosphide (MnP) films near the ferromagnetic-to-helimagnetic (FM–HM) transition. MnP films (~100 nm thick, grain size ~86 nm) were grown on Si substrates using molecular beam epitaxy, followed by deposition of Fe_3O_4 layers of varying thicknesses (7 nm and 58 nm). The results show that a thin Fe_3O_4 layer (7 nm) enhances interfacial magnetic coupling and overall magnetization in the bilayer, while the thicker Fe_3O_4 layer (58 nm) dominates the magnetic response due to its soft magnetic nature. Remarkably, the MR near the FM–HM transition increases by 20% and 37% with the 7 nm and 58 nm Fe_3O_4 layers, respectively, attributed to strain-enhanced spin-dependent scattering at the interface. These findings provide new insights into strain-modulated magnetic coupling at iron oxide/helimagnet interfaces and underscore their potential for advanced spintronic applications.

Received 26th June 2025,
Accepted 14th November 2025

DOI: 10.1039/d5nr02716k

rsc.li/nanoscale

Introduction

Helimagnetism is a type of magnetic order characterized by a non-collinear arrangement of spins, resulting in a helical or spiral structure.[1–3] In helimagnets, the magnetic moments of the atoms rotate continuously, forming a helix along a specific axis. This configuration can support the formation of topological spin textures, such as skyrmions.[4,5] This contrasts with ferromagnetism, where spins are aligned parallel, and antiferromagnetism, where they align antiparallel. Helimagnetism presents a rich area of study in condensed matter physics, with implications for both fundamental research and practical applications.[6–10]

Helimagnets can be utilized in spintronic devices, which exploit the spin of electrons for information processing and storage, potentially leading to faster and more efficient technologies.[11–14] Their unique magnetic configurations may enhance data storage solutions, allowing for higher density and faster access times in hard drives and memory devices.[2] Additionally, helimagnets can be employed in highly sensitive magnetic sensors, benefiting applications in industrial, automotive, and consumer electronics.

Magnetoresistance (MR) is a key principle in spintronic devices, leveraging both the charge and spin of electrons to create more efficient electronic components, including memory and logic circuits.[15] Materials exhibiting large MR are crucial for developing energy-efficient devices, which is particularly important for reducing power consumption in electronic applications. Investigating magnetoresistance in helimagnets opens new avenues for research and applications, making it a critical area in materials science and condensed matter physics.[16–18] The unique magnetic properties of heli-

[a]*Department of Physics, University of South Florida, Tampa, Florida 33620, USA. E-mail: nivarthanawa@usf.edu, phanm@usf.edu*
[b]*Department of Energy Conversion and Storage, Technical University of Denmark, 2800 Kgs. Lyngby, Denmark*
[c]*Faculty of Materials Science and Engineering, Phenikaa University, Hanoi 12116, Vietnam*
[d]*Center for Materials Innovation and Technology, VinUniversity, Hanoi 100000, Vietnam*

magnets have been predicted to result in enhanced MR effects in the helimagnetic regime compared to ferromagnetic materials,[19] potentially enhancing the efficiency and sensitivity of sensors and memory devices.

Helimagnetic phenomena have been observed in a variety of magnetic systems, such as MnSi,[20] MnP,[21,22] MnGe,[23] $MnAuS_2$,[14] $DyTe_3$,[24] CrI_2,[25] $Cr_{1/3}NbS_2$,[26–28] $Fe_xCo_{1-x}Si$[29] and FeGe.[30] However, a comprehensive understanding of their properties has remained elusive. Among these, manganese phosphide (MnP) has garnered significant attention due to its multifunctional magnetic, superconductive, thermoelectric, magnetocaloric, and magnetoresistive properties.[13,31–34] Bulk MnP exhibits a complex magnetic phase transition, transitioning from paramagnetic (PM) to ferromagnetic (FM) at $T_C \approx 291$ K, followed by an FM to helimagnetic (HM) transition at $T_N \approx 47$ K.[34] Nanostructuring has been reported to considerably alter the HM behavior in MnP, with notable increases in the FM–HM transition temperature (up to 110 K) in nanocrystalline films.[22,35] The unique magnetic behavior of MnP, driven by the Dzyaloshinskii–Moriya interaction (DMI), makes it a promising candidate for emergent magnetism and magnetotransport in heterostructure systems.

In a recent study, we discovered a large magnetoresistance effect in MnP nanostructured films near the FM–HM transition by leveraging confinement, strain effects, and spin helicity.[36] This highlights a novel strain-mediated spin helicity phenomenon in nanostructured helimagnets, presenting a promising pathway for developing high-performance magnetoresistive sensors and spintronic devices. Further research into such nanostructured helimagnets and their heterostructures, formed by interfacing MnP with other functional magnetic materials, may lead to new materials with tailored properties for specific applications in electronics and materials science.

In this context, iron oxide (Fe_3O_4) emerges as an excellent candidate for forming heterostructures with MnP. Fe_3O_4 possesses an inverse spinel crystal structure, where O^{2-} ions are arranged in a cubic close-packed manner.[37–39] The unit cell features two distinct cation sites, referred to as A and B sites. A sites are occupied by Fe(III) ions, forming tetrahedral coordination, while B sites contain equal numbers of Fe(II) and Fe(III) ions in octahedral coordination. This structure allows magnetite to be represented as $[Fe^{3+}]_A[Fe^{2+}Fe^{3+}]_BO_4$. The electron hopping between Fe^{3+} and Fe^{2+} at the B sites enhances conductivity compared to other iron oxides like Fe_2O_3 and FeO.[37,38] Furthermore, the spins of Fe^{3+} at A sites and those of Fe^{2+} and Fe^{3+} at B sites are antiferromagnetically coupled *via* superexchange, giving Fe_3O_4 its ferrimagnetic properties.[37] Fe_3O_4 also exhibits a high Curie temperature (~860 K) and high spin polarization (~100%), making it desirable for spintronics applications.[40] At room temperature, Fe_3O_4 behaves as a semiconductor, transitioning to an insulating state around 120 K *via* the Verwey transition, which is accompanied by a structural transformation from cubic inverse spinel to a monoclinic phase.[37,38,41] A substantial body of research has focused on the magnetic, multiferroic, magnetoresistive, and spin-thermo-transport properties of Fe_3O_4 films and heterostructures, which aim to explore them for applications in spintronics and spin-caloritronics.[40,42–47]

The formation of Fe_3O_4/MnP interfaces in bilayer structures is expected to lead to novel magnetic and magneto-transport phenomena due to proximity and exchange coupling effects, as well as structural modifications at the interface.[40,42,46] Structural changes around the Verwey transition of Fe_3O_4 may significantly impact the Fe_3O_4/MnP interface coupling and the higher MR behavior of MnP nanostructured films near the FM–HM transition temperature. Using techniques such as X-ray diffraction (XRD), atomic force microscopy (AFM), magnetic force microscopy (MFM), and temperature- and magnetic field-dependent magnetometry and resistivity, our study sheds light on the emergent magnetic and magnetoresistance phenomena in Fe_3O_4/MnP heterostructures. We demonstrate that the presence of a Fe_3O_4 layer can increase the MR effect by 13% in Fe_3O_4/MnP bilayers, with the MR ratio tunable by varying Fe_3O_4 thickness. By introducing the "universal curve" analytical method, we show that the intrinsic transport properties of MnP in the helimagnetic state are consistent across samples, regardless of Fe_3O_4 thickness. Our findings pave the way for developing novel heterostructures based on nanostructured helimagnets with enhanced MR properties, meeting the increasing demands of modern spintronic and sensor devices.

Results and discussion

Structural characterization

Since the structural properties of the MnP films used in this study were thoroughly characterized in our previous work,[36] we present here those of Fe_3O_4 layers (thickness, ~7 and ~58 nm) deposited on top of the MnP films (average grain size of ~86 nm, film thickness ~100 nm) and Fe_3O_4/MnP bilayers. For thickness determination, part of the MnP film was masked during PLD growth of Fe_3O_4 to leave a bare reference region of MnP. The AFM step-height across this boundary was measured and the resultant profile is shown in Fig. S1. Presence of Fe and O on MnP films were investigated by EDS. Fig. S2 shows the obtained EDS spectra for Fe_3O_4/MnP bilayers. Fig. 1a shows the XRD pattern of the Fe_3O_4 (58 nm)/MnP bilayer, with reference to those of the MnP and Fe_3O_4 films. We observed the characteristic peaks of Fe_3O_4 phase, specifically the (1 1 1), (3 1 1), (2 2 2), and (5 1 1) reflections, which are consistent with the Fe_3O_4 films grown on Si substrates. Additionally, the Fe_3O_4 (58 nm)/MnP film displays (4 0 0) of Fe_3O_4 phase, which is absent in Fe_3O_4 (62 nm)/Si film. Several diffraction planes of MnP phase are present in the Fe_3O_4 (58 nm)/MnP bilayer, confirming that the MnP retains its orthorhombic structure (*Pnma* space group) with lattice parameters of a = 5.259 Å, b = 3.173 Å, and c = 5.917 Å. Both Fe_3O_4 films, deposited on Si and MnP, exhibit a face-centered cubic lattice structure with $Fd\bar{3}m$ and $F\bar{4}3m$ space groups. The lattice parameters for Fe_3O_4 (62 nm)/Si and Fe_3O_4 (58 nm)/MnP/Si are a = 8.3963 Å and a =

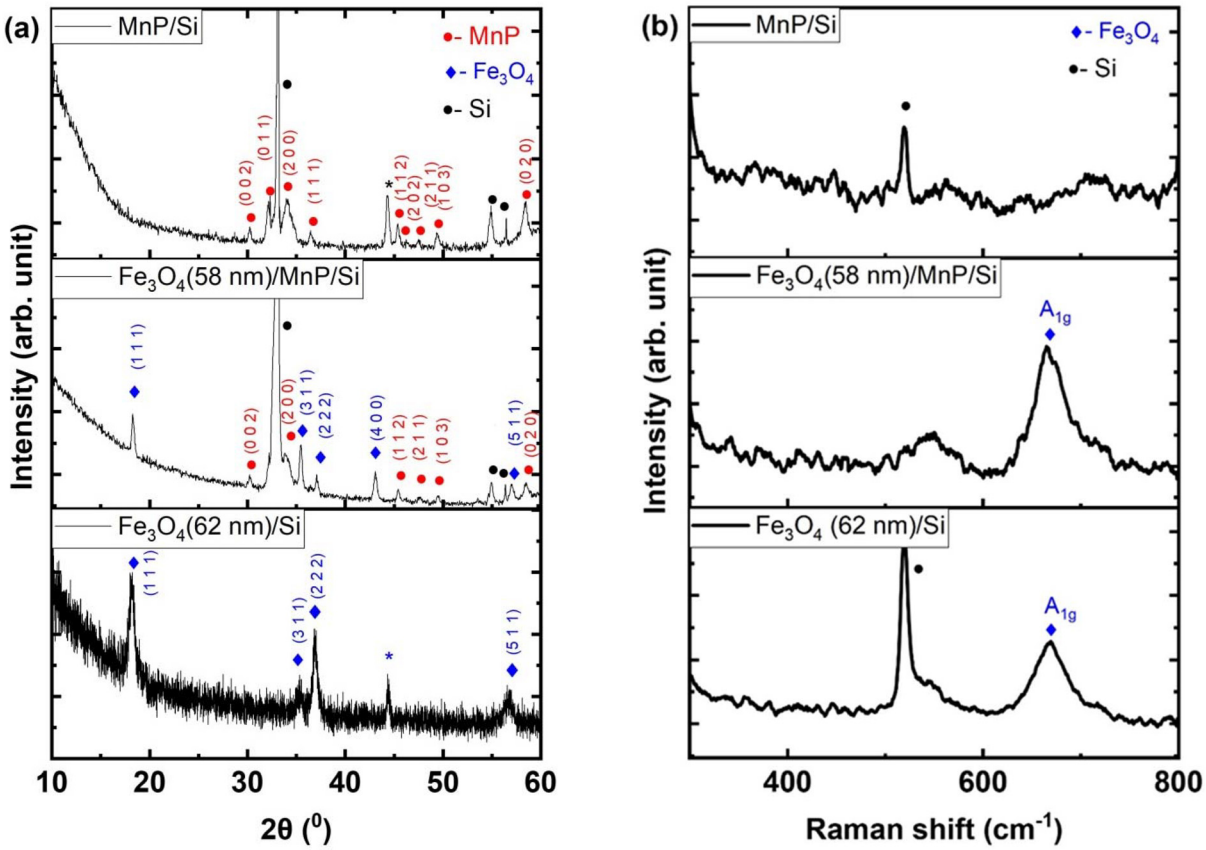

Fig. 1 (a) X-ray diffraction (XRD) patterns of MnP/Si, Fe_3O_4 (58 nm)/MnP, and Fe_3O_4 (62 nm)/Si. The asterisk mark (black) indicates the XRD signal from the sample holder and the asterisk (blue) is due to Si substrate. (b) Raman spectra of MnP/Si, Fe_3O_4 (58 nm)/MnP, and Fe_3O_4 (62 nm)/Si.

8.3941 Å, respectively. This indicates that the substrate plays a critical role in the growth of Fe_3O_4 thin films.[37,48] Fig. 1b shows the room temperature Raman spectra of MnP/Si, Fe_3O_4 (58 nm)/MnP/Si, and Fe_3O_4 (62 nm)/Si samples. Raman active modes of A_{1g} of Fe_3O_4 in the Fe_3O_4/MnP bilayers and Fe_3O_4/Si are observed at 667 cm^{-1} (668 cm^{-1}). The peak positions of the Raman spectra are basically consistent with the previously reported data of Fe_3O_4 films.[49–51] No additional iron oxide phases were detected in the Raman spectra.

Topography images of Fe_3O_4 (7 nm)/MnP and Fe_3O_4 (58 nm)/MnP are displayed in Fig. 2(a and b). The root mean square (RMS) roughness was determined to be 6.1 nm and 3.4 nm, respectively, for the 7 nm and 58 nm Fe_3O_4 films on MnP. The bare MnP film exhibited a roughness of 6.5 nm. Luo *et. al* have shown the correlation between the thickness of graphene and the surface morphology of the substrate when depositing graphene on Cu using chemical vapor deposition method.[52] Notably, in our study the intended thickness of this deposition was ~80 nm based on the calibrated thickness of Fe_3O_4 on Si substrate (~83 nm), even using the exact same deposition conditions. This discrepancy suggests a difference in the growth mechanism of Fe_3O_4 on MnP compared to that on Si. This substrate roughness of MnP (6.5 nm) could explain the deviation in film thickness from the calibrated thickness, as the Fe_3O_4 (58 nm)/MnP film exhibits roughly half the roughness of the MnP film. This suggests that during initial nucleation and growth, the Fe_3O_4 fills voids on the MnP surface. Conversely, Fe_3O_4 on Si showed a significantly lower roughness of 0.1 nm. Fe_3O_4 reference films were also deposited on Si substrates. The target thicknesses were chosen to match as closely as possible the Fe_3O_4 layers grown on MnP (7 nm and 58 nm). Due to minor variations in PLD chamber conditions and uncertainties in thickness measurement, the resulting Fe_3O_4/Si reference films were ~10 nm and ~62 nm. These samples are reported throughout the manuscript as Fe_3O_4/Si references. It is generally accepted that the grain size of a thin film grows when the film thickness increases.[53] Our Fe_3O_4/Si films also demonstrated this, as indicated by the AFM topography images, Fig. S3(a–c). In contrast, the Fe_3O_4 (7 nm)/MnP/Si shows a random size distribution of grain sizes from large to small (inset of Fig. 2a and Fig. S4a) when compared to Fe_3O_4 (58 nm)/MnP/Si (inset of Fig. 2b and Fig. S4b).

Magnetic force microscopy analysis

MFM measurements were conducted on all samples at room temperature, including Fe_3O_4 (10 nm and 62 nm) on Si, MnP (100 nm) on Si, and their Fe_3O_4/MnP bilayers. Fig. 2(c and d) presents MFM images of Fe_3O_4 (58 nm)/MnP/Si, revealing

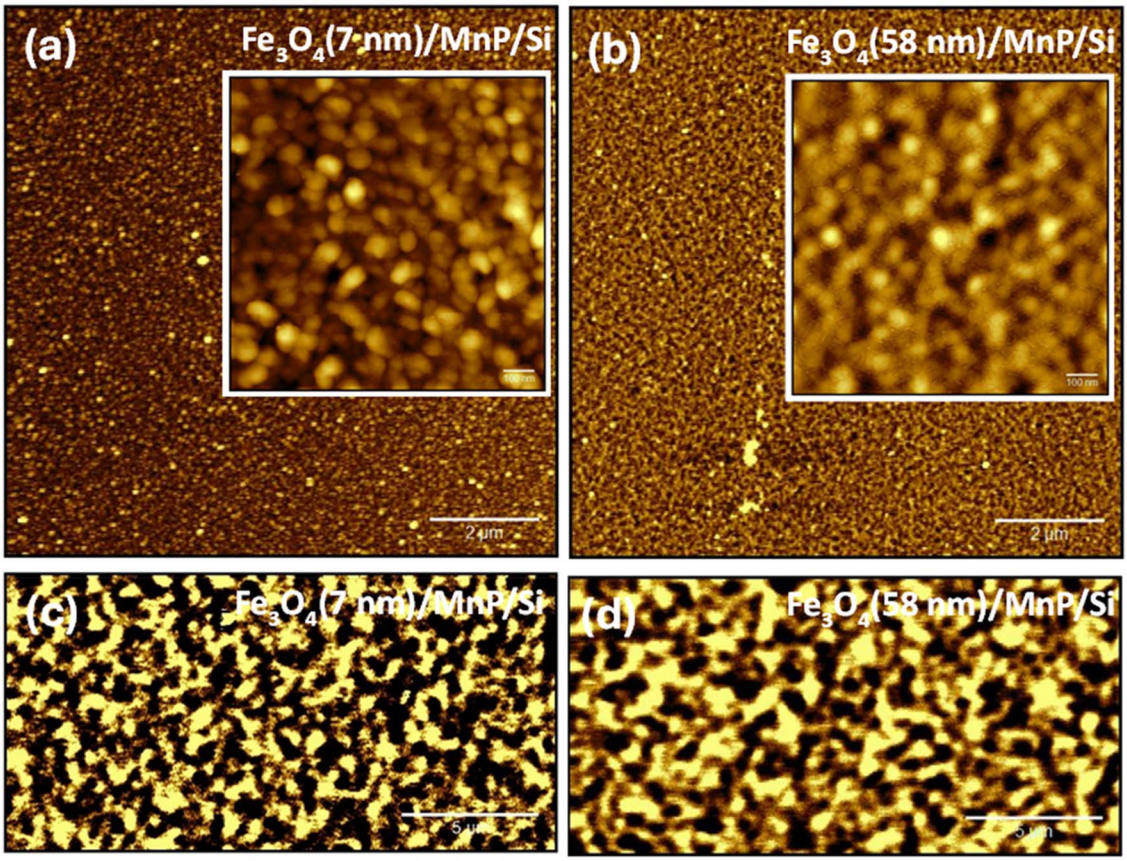

Fig. 2 Atomic force microscopy (AFM) topography images of (a) Fe_3O_4 (7 nm)/MnP/Si and (b) Fe_3O_4 (58 nm)/MnP/Si; room temperature magnetic force microscopy (MFM) images of (c) Fe_3O_4 (7 nm)/MnP/Si and (d) Fe_3O_4 (58 nm)/MnP/Si.

bright and dark contrasts that indicate the presence of randomly distributed magnetic domains. These domains are aligned perpendicularly to the plane of the film. The domain distribution of Fe_3O_4 (58 nm)/MnP/Si is comparable to that observed in the Fe_3O_4 (62 nm)/Si film (Fig. S5a). Similar magnetic domain patterns in Fe_3O_4 films grown on $SrTiO_3$:Nb using PLD were reported by Wei *et al.*[54] In MFM, the contrast in the domain image arises from the magnetic force gradient $\left(\frac{dF}{dz}\right)$ between the sample and the MFM tip, which is proportional to the stray field of the film.[55] The root-mean-square (RMS) value of phase shift ($\Delta\phi_{RMS}$) is defined as $\Delta\phi_{RMS} = \frac{Q}{K}\left(\frac{dF}{dz}\right)$, where Q is the quality factor and K is the spring constant of the tip.[56,57] The Q value, K, and lift height were kept constants for all measurements to ensure valid comparisons of the $\Delta\phi_{RMS}$ values across the bilayers and reference films. At 300 K, the measured $\Delta\phi_{RMS}$ values were 0.6399 for Fe_3O_4 (7 nm)/MnP, 0.8190 for Fe_3O_4 (58 nm)/MnP, 0.3532 for MnP/Si, 1.1160 for Fe_3O_4 (62 nm)/Si, and 0.1160 for Fe_3O_4 (10 nm)/Si (Fig. S5d). These variations in $\Delta\phi_{RMS}$ reflect differences in the $\frac{dF}{dz}$ and consequently, the underlying magnetic domain structures and stray field strength. Notably, the thinner layer (7 nm) of Fe_3O_4 on MnP shows a higher $\Delta\phi_{RMS}$ value when compared to the Fe_3O_4 (10 nm) film grown on Si (0.1160), indicating that MnP influences the magnetic properties of the Fe_3O_4 layer in Fe_3O_4/MnP.[58]

Since MFM is a surface-sensitive technique, the magnetic contrast and RMS phase shift values primarily reflect the magnetic properties of the uppermost layers, with the Fe_3O_4 top layer dominating the signal in the Fe_3O_4/MnP bilayer samples. Comparing the Fe_3O_4/MnP bilayers with the bare MnP film shows a stronger magnetic signal due to significant stray fields of Fe_3O_4. When comparing the Fe_3O_4/MnP bilayers to Fe_3O_4/Si films, differences in $\Delta\phi_{RMS}$ values arise from the distinct growth behaviors on each substrate. Growth of Fe_3O_4 on MnP introduces unique magnetic domain structures, possibly due to strain, crystallographic orientation, or interfacial exchange coupling. These effects are less significant in Fe_3O_4 films grown on Si, where the magnetic domains follow a more typical Fe_3O_4 pattern (Fig. S5b) when compared to Fe_3O_4 on MnP (Fig. 2c). The MnP substrate likely alters the Fe_3O_4 growth process, affecting domain size, or magnetic anisotropy, which in turn impacts $\Delta\phi_{RMS}$.[58] The influence of sitall-substrate roughness on Ta_2O_5 film growth mechanisms was studied by Sergeev *et al.*, showing that the roughness of sitall-substrates could lead to different sizes of grains and increased

intergranular stress.[48] Rougher substrates may also reduce the thickness of the upper layer by enhancing surface diffusion and atom migration, leading to the filling of valleys and smoothing of peaks. This explains the deviation in thickness of the Fe_3O_4 films grown on Si and MnP. The rough surface of MnP significantly influenced the growth of the Fe_3O_4 (7 nm) film and its resulting magnetic properties, in contrast to the Fe_3O_4 (10 nm) film grown on a smooth Si substrate. The difference in grain size observed in Fe_3O_4 (7 nm)/MnP/Si (inset of Fig. 2a) and its higher $\Delta\phi_{RMS}$, as compared to Fe_3O_4 (10 nm)/Si (Fig. S3c), further support this conclusion. On another note, the deposition of the Fe_3O_4 (7 nm) layer on the rough surface of MnP may influence the magnetic behavior of the MnP film. A dual magnetic proximity effect, arising from the interactions between the MnP and Fe_3O_4 layers, likely contributed to the observed magnetic properties of the Fe_3O_4/MnP bilayers.[59–61] In contrast, for the Fe_3O_4 (58 nm)/MnP bilayers, the thicker Fe_3O_4 layer predominated the system's magnetism, leading to similar trends in both $\Delta\phi_{RMS}$ and M_S of the Fe_3O_4 (58 nm)/MnP and Fe_3O_4 (62 nm)/Si configurations.

Magnetometry analysis

To understand the impact of Fe_3O_4 deposition on the magnetic properties of MnP thin films, we conducted systematic temperature- and magnetic field-dependent magnetization measurements on all samples, including Fe_3O_4 (7 nm and 58 nm) on Si, MnP(100 nm) on Si, and their Fe_3O_4/MnP bilayers, using the vibrating sample magnetometry (VSM) option of the physical property measurement system (PPMS). Fig. 3(a and b) shows the temperature dependence of in-plane DC magnetization (M–T) of Fe_3O_4 (7 nm)/MnP/Si and Fe_3O_4 (58 nm)/MnP/Si films measured under zero-field-cooled (ZFC), field-cooled-cooling (FCC), and field-cooled-warming (FCW) protocols in presence of a magnetic field 0.1 T. The magnetization behavior of the Fe_3O_4/MnP bilayers exhibits significant differences in the lower temperature region (<100 K) compared to the bare MnP film (inset of Fig. 3a). Notably, the M–T curves under ZFC indicate the larger magnetization values at 300 K for Fe_3O_4 (7 nm)/MnP/Si (~63 emu cm^{-3}) and Fe_3O_4 (58 nm)/MnP/Si (~315 emu cm^{-3}) than for MnP (~17 emu cm^{-3}). The M_S of the three films also follows the same trend of the magnetization at 300 K, as indicated in Fig. S5e. This reinforces the interaction between the two materials in the bilayer structure, which arises from the dual magnetic proximity effect.[60] The temperature-dependent magnetization trend at higher temperatures (>200 K), continues to align with the bare MnP film. In contrast, the Fe_3O_4 layers impact the magnetization profile of the MnP, particularly at low temperatures (<200 K). The first derivative of the M–T dependence of the Fe_3O_4/MnP bilayers shows that the paramagnetic to ferromagnetic (PM–FM) transition of MnP (T_C ~306 K) remains nearly unchanged, appearing at ~304 K for Fe_3O_4 (7 nm)/MnP and ~302 K for Fe_3O_4 (58 nm)/MnP (Fig. S6a). However, the ferromagnetic to helimagnetic (FM–HM) transition of MnP, typically observed around T_N ~102 K, shifts to lower temperatures (~90 K) in the Fe_3O_4/MnP bilayers. It should be noted that the Verwey temperature (T_v), which was observed at approximately 118 K in our Fe_3O_4/Si samples (Fig. S6b), where a noticeable slope change in magnetization occurred in the M–T curve. This value is close to the Verwey transition temperature of bulk Fe_3O_4 (T_v ~120 K).[37] It is important to note that the presence of the Fe_3O_4 layer on the MnP film had a negligible impact on the PM–FM transition of MnP (approximately 300 K) but resulted in a shift of the FM–HM transition to a lower temperature (~90 K) (Table S1). In the present bilayer system, however, we find no noticeable shift in the PM–FM transition around 300 K, suggesting that the static strain from the Fe_3O_4 overlayer is insufficient to modify MnP's high-T ordering. By contrast, the structural transformation of Fe_3O_4 during its Verwey transition (~110–120 K) imposes a transient interfacial strain, which is capable of perturbing the MnP layer and shifting its low-temperature FM–HM transition. Additionally, previous reports have highlighted the varying effects of strain (whether tensile or compressive) on the FM–HM transition of MnP. Choi *et al.* observed an increase in T_N (approximately 100 K) in MnP films, attributing this change to strain effects resulting from the lattice mismatch between the epitaxial MnP film and the GaAs substrate.[62] Similarly, de Andrés *et al.* reported a significant increase in T_N from 47 K for bulk MnP to 67 K for MnP films grown on GaP substrates, and 82 K for MnP nanocrystals embedded in GaP epilayers, while the T_C values remained largely unchanged.[63] They suggested that surface strains induced by tensions in the MnP nanocrystals substantially modify the helimagnetic structure, leading to the observed increase in T_N. In contrast, Sun *et al.* found a slight decrease in T_N (~38 K) for a 2D MnP single crystal compared to its 3D bulk counterpart (~47 K).[32] Gregg *et al.* reported complete suppression of T_N in 20 nm orthorhombic MnP nanorods with their growth direction along the *b*-axis, suggesting that the screw phase was entirely confined along the hard *a*-axis.[64] Hirahara *et al.* demonstrated that applying tensile strain along the *a*-axis of a MnP single crystal favored antiferromagnetic (AFM) interactions over ferromagnetic (FM) ones, resulting in the increased T_N and decreased T_C. Conversely, compressive strain along the *c*-axis produced the opposite effects, yielding lower T_N and higher T_C values.[65] In the present study, the increase in T_N of the MnP nanocrystalline film (~102 K), compared to bulk MnP (~47 K), is attributed to surface strains induced by tension resulting from the nanostructuring effect. The deposition of the Fe_3O_4 layer on the MnP film appears to weaken the influence of these surface strains on the FM–HM transition, thereby reducing the T_N of the MnP film. Additionally, the magnetic proximity effect induced by the Fe_3O_4 layer could significantly contribute to the interfacial magnetic coupling between the two layers, as indicated by the MFM analysis.

To further clarify this, we measured the magnetic field-dependent magnetization (M–H) curves across a broad temperature range of 10 to 350 K for all samples, including MnP/Si, Fe_3O_4 (10 nm)/Si, Fe_3O_4 (62 nm)/Si, Fe_3O_4 (7 nm)/MnP/Si, and Fe_3O_4 (58 nm)/MnP/Si. A comprehensive analysis of these data

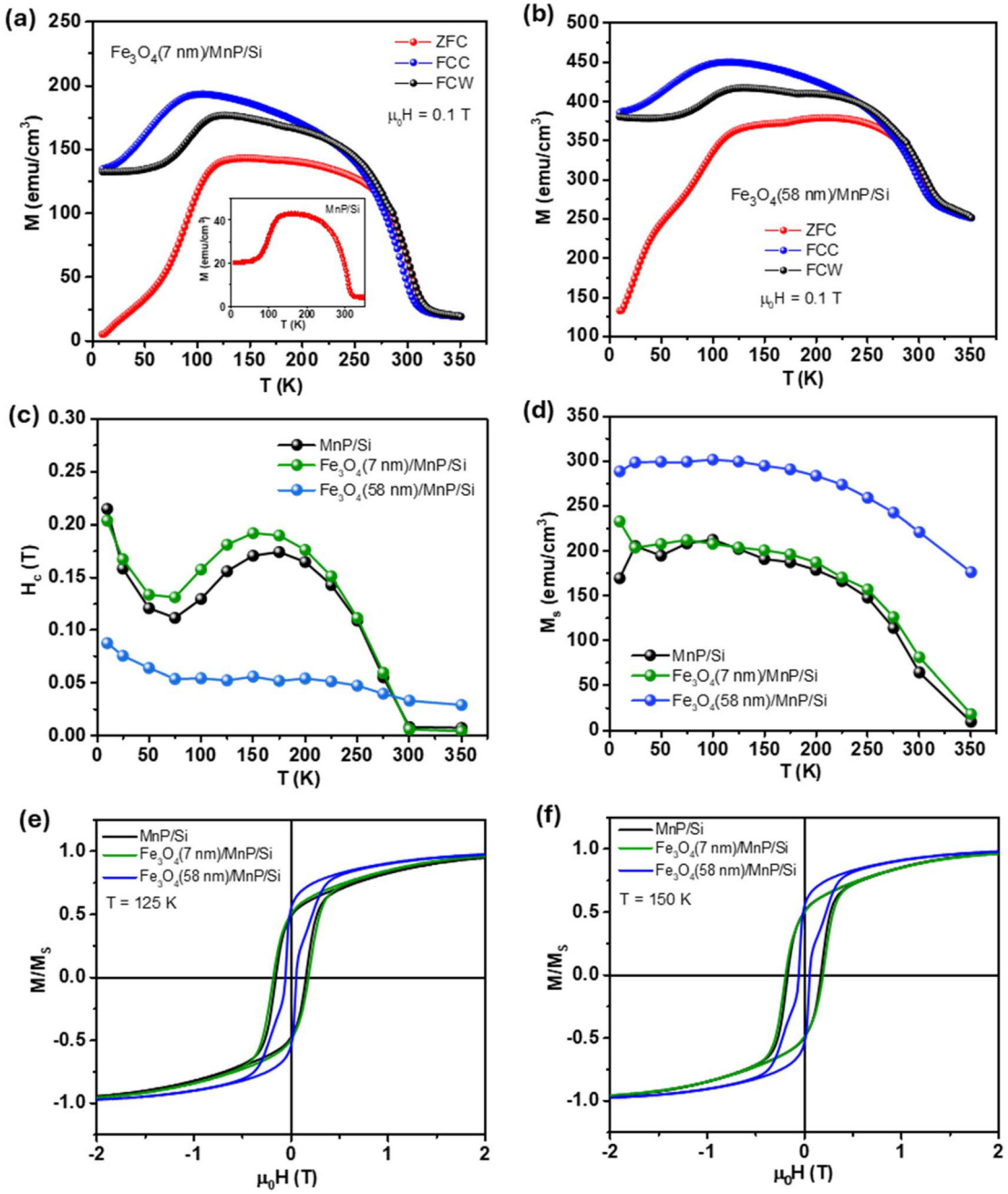

Fig. 3 Temperature dependence of in-plane magnetization (M–T) of (a) Fe_3O_4 (7 nm)/MnP/Si and (b) Fe_3O_4 (58 nm)/MnP/Si. The inset of (a) represents the M–T dependence of MnP/Si under ZFC protocol at 0.1 T; temperature dependence of (c) coercivity (H_C) and (d) saturation magnetization for the three films; magnetic field-dependent magnetization (normalized) for the three films at (e) 125 K and (f) 150 K for the in-plane (IP) configuration.

reveals that the presence of the Fe_3O_4 (7 nm) layer significantly enhanced the coercivity (H_C) of Fe_3O_4 (7 nm)/MnP compared to the bare MnP film, particularly within the temperature range of 50–250 K where the Verwey transition of Fe_3O_4 (~118 K) and the FM–HM transition of MnP (~102 K) occurred; a similar temperature-dependent coercivity trend was observed for both cases though (see Fig. 3c). The temperature-dependent saturation magnetization of Fe_3O_4 (7 nm)/MnP/Si is comparable with MnP/Si with a small increment throughout the temperature region of 10–350 K (see Fig. 3d). On the other hand, the highest M_S of Fe_3O_4 (58 nm)/MnP/Si supports the prominent effect of Fe_3O_4 when the layer thickness increased. In the temperature regime of interest (50–250 K), the shape of the M–H loops for the Fe_3O_4 (7 nm)/MnP bilayer closely resembles that of the bare MnP film (see Fig. 3(e and f)). These findings suggest that the presence of a

thin layer of Fe_3O_4 enhances magnetic coupling at the Fe_3O_4/MnP interface, contributing to the overall enhanced magnetism of the system (Fig. 3c and d). The situation is notably different for the Fe_3O_4 (58 nm)/MnP bilayer, where the presence of the 58 nm-thick Fe_3O_4 layer, exhibiting soft ferromagnetic characteristics (see Fig. S6(c and d)), dominates the overall magnetism of the system. This results in a significant reduction in H_C and a low-field shrinking loop shape at temperatures below the T_C of MnP (Fig. 3(e and f)).

Transport and magnetoresistance properties

To understand the effect of Fe_3O_4 deposition on the transport and magnetoresistance properties of the MnP films, we conducted temperature and magnetic field-dependent resistivity measurements on the bare MnP film and Fe_3O_4/MnP bilayers over a wide temperature range of 10–300 K. Fig. 4a illustrates the temperature dependence of the longitudinal resistivity (ρ) for MnP/Si, Fe_3O_4 (7 nm)/MnP/Si, and Fe_3O_4 (58 nm)/MnP/Si films measured in zero magnetic field. A clear distinction is observed between the resistivity profiles of the bilayer films and the bare MnP film. The resistivity of MnP exhibits metallic behavior, with a gradual decrease in resistivity as the temperature decreases to approximately 110 K. The minimum around 97 K, followed by an upturn (maximum at approximately 73 K), is observed and attributed to the confinement and strain effects, as well as magnetic phase coexistence and competition in governing electron transport properties.[36] In the Fe_3O_4-deposited MnP films, this resistivity minimum shifted to lower temperatures, specifically to ~85 K for Fe_3O_4 (7 nm)/MnP/Si and ~69 K for Fe_3O_4 (58 nm)/MnP/Si. Additionally, the peak of the resistivity upturn, which occurred around 73 K in MnP/Si, shifted to about 61 K for Fe_3O_4 (7 nm)/MnP/Si and 45 K for Fe_3O_4 (58 nm)/MnP/Si. These shifts suggest that the presence of the Fe_3O_4 layer significantly altered the electronic transport properties of MnP, particularly in the low-temperature regime. Guan *et al.* observed the effect of a capping layer (Fe_3O_4) on the metal–insulator transition of $La_{0.7}Ca_{0.3}MnO_3$ films due to the $Fe_3O_4/La_{0.7}Ca_{0.3}MnO_3$ interface effect.[66] Furthermore, Takahashi *et al.* noted an increase in resistivity with increasing Fe_3O_4 thickness when grown on a metallic spacer layer, Au, attributed to the interface between Fe_3O_4 and the metallic spacer.[67] In our study, we found that the overall resistivity of the Fe_3O_4/MnP bilayers increased with the thickness of the Fe_3O_4 layer.

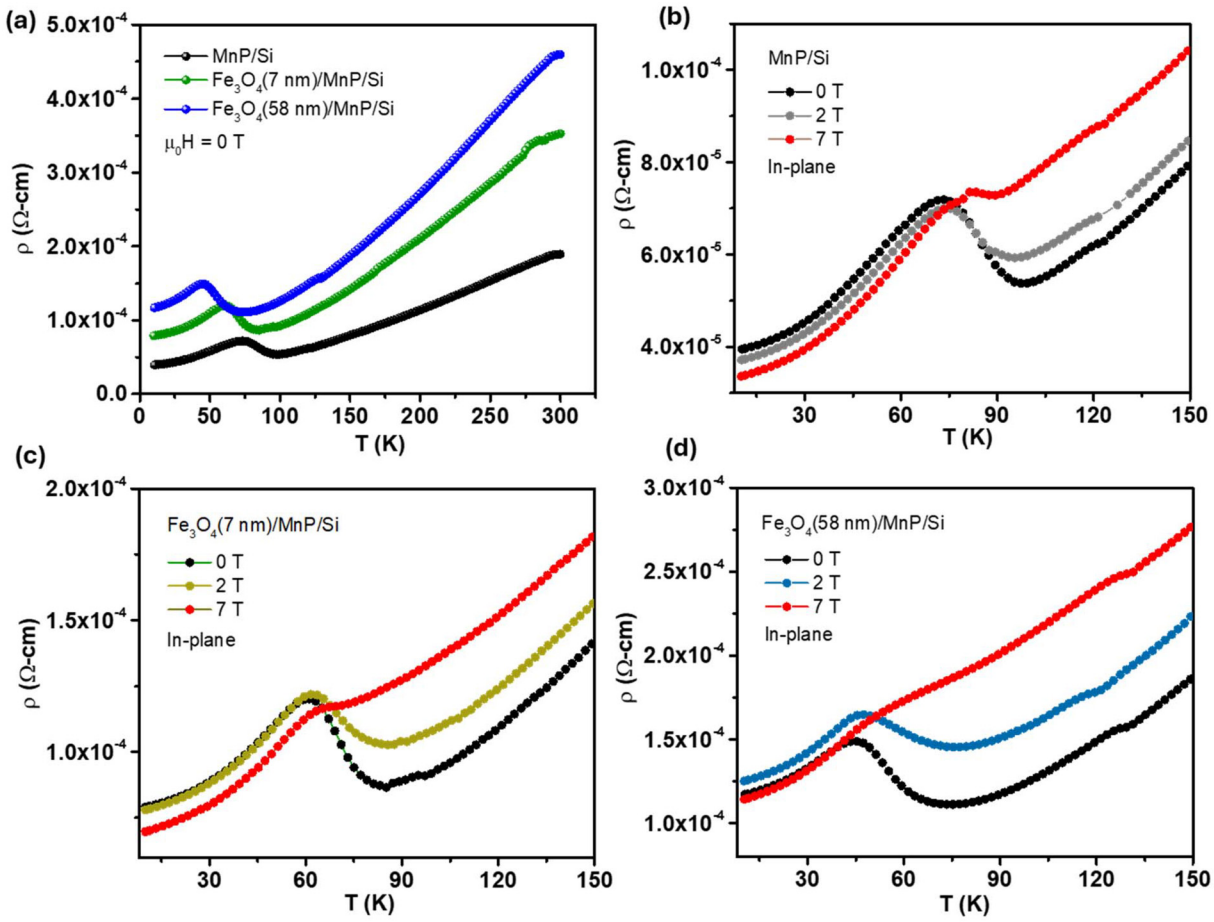

Fig. 4 (a) The temperature-dependent resistivity under zero field for MnP/Si and Fe_3O_4/MnP/Si samples; longitudinal resistivity under in-plane magnetic fields of 0, 2, and 3 T within an enlarged temperature range of 8–150 K for (b) MnP/Si, (c) Fe_3O_4 (7 nm)/MnP/Si, and (d) Fe_3O_4 (58 nm)/MnP/Si.

Fig. 4(b–d) shows $\rho(T)$ under magnetic fields of 0, 2, and 7 T across a temperature range of 10–150 K for MnP, Fe_3O_4 (7 nm)/MnP/Si, and Fe_3O_4 (58 nm)/MnP/Si. It is interesting to note that for the bare MnP film, the application of magnetic fields enhanced the resistivity at temperatures above approximately 75 K, while reducing it at lower temperatures (Fig. 4b). This effect becomes even more pronounced with the application of higher magnetic fields. A similar trend is observed for the Fe_3O_4 (7 nm)/MnP bilayer (Fig. 4c), although the effects are more pronounced due to the presence of the deposited Fe_3O_4 (7 nm) layer. The case is different for the Fe_3O_4 (58 nm)/MnP bilayer (Fig. 4d), where the effects of applied low (2 T) and high (7 T) magnetic fields on resistivity differ significantly. The application of a 2 T field increased the resistivity across the entire temperature range of 10 to 300 K. In contrast, the 7 T field raised the resistivity at temperatures above 50 K but reduced it at lower temperatures. This indicates that the magnetic fields have varying impacts on the magneto-transport properties of Fe_3O_4/MnP bilayers depending on the thickness of the Fe_3O_4 layer.

To further clarify this intriguing feature, we have performed a thorough analysis of the MR data and display in Fig. 5 the magnetic field-dependent MR profiles of the Fe_3O_4/MnP bilayers, with reference to the MR profile of the bare MnP film (Fig. S7). It can be observed that the Fe_3O_4 (7 nm)/MnP bilayer shows a sign change of MR from positive to negative at ~65 K (see Fig. 5a and 6a), while the Fe_3O_4 (58 nm)/MnP bilayer exhibits this sign change at ~50 K (see Fig. 5b and 6a). Such changes in MR sign resemble those of the bare MnP film, where the MR sign change occurred at approximately 75 K (Fig. S7). This sign change in the MnP film has been attributed to the confinement and strain effects within the FM regime of the MnP nanostructured film, which govern the transport properties and lead to the positive MR behavior in this region.[36] The MR magnitude reaches its maximum at approximately 102 K, which corresponds to the FM–HM transition temperature of the MnP film (Fig. 6). The spin-dependent scattering mechanisms at the grain boundaries in the MnP polycrystalline film are thought to be responsible for the positive MR effect. It is noteworthy that the presence of the Fe_3O_4 layer significantly enhances the positive MR effect of the bare MnP film, with the magnitude of MR increasing as the thickness of the Fe_3O_4 layer increases. The maximum MR ratio of the bare MnP film increases by 20% with the 7 nm Fe_3O_4 layer and by 37% with the 58 nm Fe_3O_4 layer in the Fe_3O_4/MnP bilayers. This enhancement in MR is attributed to proximity-enhanced spin-dependent scattering at the Fe_3O_4/MnP interface.[40] This enables us to interpret the further enhancement of the MR

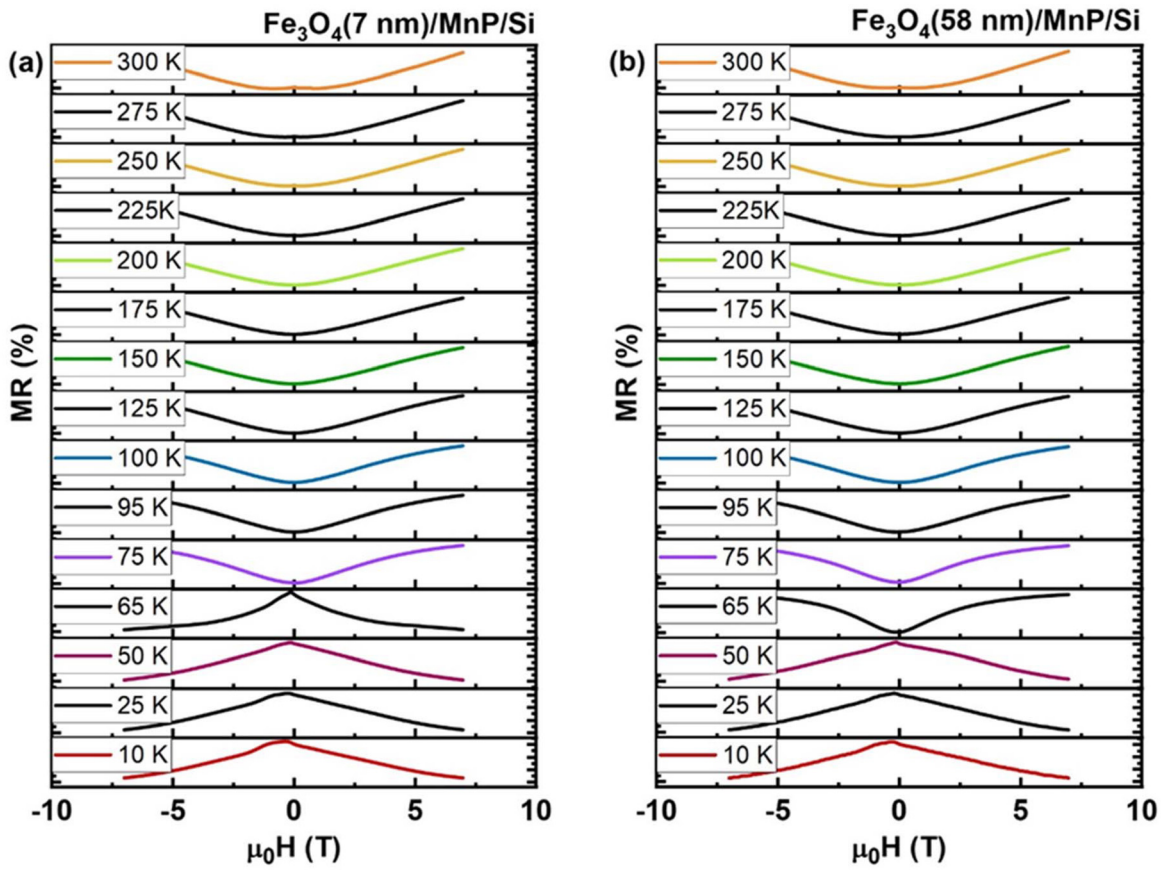

Fig. 5 In-plane (IP) magnetic field-dependent longitudinal magnetoresistance (MR) for (a) Fe_3O_4 (7 nm)/MnP/Si and (b) Fe_3O_4 (58 nm)/MnP/Si.

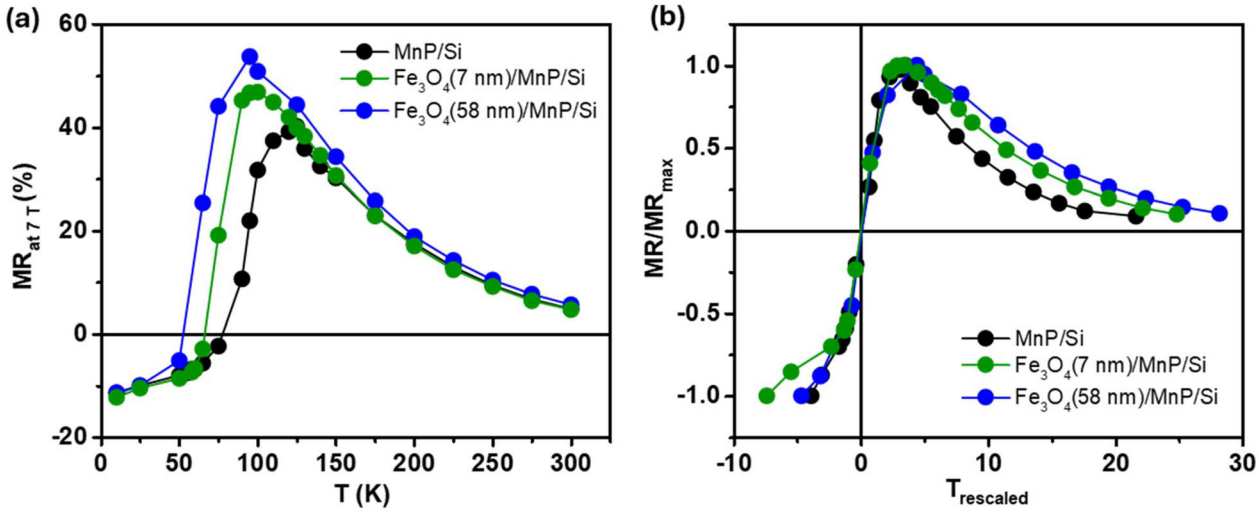

Fig. 6 (a) Temperature-dependent longitudinal magnetoresistance (MR) ratio at 7 T for MnP/Si, Fe_3O_4 (7 nm)/MnP/Si, and Fe_3O_4 (58 nm)/MnP/Si under an in-plane magnetic field and (b) the rescaled temperature-dependent normalized MR for the three films.

ratio for Fe_3O_4/MnP/Si compared to MnP/Si when the applied magnetic field is perpendicular to the plane of the film (referred to as out-of-plane (OP) MR) (Fig. S8a), in comparison with the in-plane (IP) MR case (Fig. 6a).

Furthermore, it is important to note that the peak of the MR(T) for the bare MnP film significantly shifts to lower temperatures in the Fe_3O_4-deposited MnP films. Increasing the thickness of the Fe_3O_4 layer further shifts the MR peak to even lower temperatures (Fig. 6). However, the overall MR(T) dependence retains a similar trend for all the samples. This might indicate the intrinsic transport characteristics of the MnP nanocrystalline film in the helimagnetic regime. To validate this, we have introduced a "universal curve" analytical method by rescaling the MR ratios to their maximum values and temperatures to the transition temperatures. The transition temperature ($T_{transition}$) is defined as the point where the MR at 7 T becomes zero, with a sign change from positive to negative. The respective $T_{transition}$ values for MnP/Si, Fe_3O_4 (7 nm)/MnP, and Fe_3O_4 (58 nm)/MnP are indicated by color boundaries in the MR(T) graphs in Fig. S8(b–d). The MR ratios (%) at 7 T were normalized with respect to their maximum values, MR (%)/MR (%)^{max}, for both the positive and negative sides of MR. This normalized data was plotted against the rescaled temperature ($T_{rescaled}$), which is defined as follows.[68]

$$T_{rescaled} = -\left(\frac{T - T_{transition}}{T_1 - T_{transition}}\right) \quad \text{for } T \le T_{transition}$$

$$T_{rescaled} = \left(\frac{T - T_{transition}}{T_2 - T_{transition}}\right) \quad \text{for } T > T_{transition}$$

where T_1 and T_2 are the reference temperatures fulfilling the criteria, $\left(\frac{T - T_{transition}}{T_1 - T_{transition}}\right) = \left(\frac{T - T_{transition}}{T_2 - T_{transition}}\right) = \text{constant} = n$, with n set to 0.5 in this study. It can be seen in Fig. 6b that the MR/MR$_{max}$ *vs.* $T_{rescaled}$ curves for all three samples nearly converge onto a single master curve in the temperature range corresponding to their respective FM–HM transition temperatures. This confirms that the intrinsic transport properties of the MnP nanocrystalline film in the helimagnetic regime are identical across the samples, regardless of FO_4 thickness. Since Fe_3O_4 exhibits higher resistivity at temperatures below the Verwey transition, when compared to MnP, it suggests that the overall resistivity of the Fe_3O_4/MnP/Si films is dominated by the MnP layer. This allows most of the current to tunnel through the Fe_3O_4 layer and pass through the metallic MnP at low temperatures (<120 K). As a result, the intrinsic transport properties of the underlying MnP layer in the helimagnetic state are revealed at temperatures below this temperature.[66]

To elucidate the underlying mechanisms driving the low-temperature MR in our system, we first examine the correlation between MR and the magnetization. As shown in Fig. S9a for the MnP/Si film measured at 10 K, the MR maximum occurs at the coercive field. The broad single-peak MR behavior (Fig. S9a), compared with the sharp features in the first derivative of the M–H loops (dM/dH, inset of Fig. S9a), indicates that the magnetoresistance arises from spin-dependent scattering averaged over domain reversal rather than from abrupt magnetization switching in MnP.[69–71] Fig. S9b shows a comparative plot of MR and $-(M/M_S)^2$ *versus* magnetic field at 10 K for MnP/Si. The strong agreement in the hysteresis behavior and peak positions confirms that the MR scales with the square of the magnetization, indicating that spin-dependent scattering is the dominant contribution to the observed negative MR.[72,73] However, when similar analysis is extended to Fe_3O_4/MnP/Si, deviations from $-(M/M_S)^2$ scaling emerge. This suggests the presence of additional transport contributions such as multi-carrier conduction or interfacial scattering, which are not captured by the spin-scattering-only picture.

Finally, to get insight into the physical mechanism(s) behind the observed magnetic field dependent transport pro-

perties of the Fe_3O_4/MnP bilayers, we have considered the semi empirical formula by Khosla and Fischer (KF) and its modification. The KF model explains the negative MR arising from spin-dependent scattering of carriers by localized magnetic moments,[74] but cannot fully capture the negative MR behavior in MnP/Si or Fe_3O_4 (7 nm)/MnP/Si. To improve the fitting, we have employed the modified KF model, as expressed in eqn (1).[36,57]

$$\mathrm{MR}(H) = -a^2 \ln(1 + b^2H^2) + \left(\frac{c^2H^2}{1 + d^2H^2}\right) \quad (1)$$

where $a = [A_1 J_{ex} D(E_F)\{S(S+1) + M^2\}]^{1/2}$, $b = \left[1 + 4\pi^2 S^2 \left(\frac{2J_{ex}D(E_F)}{g}\right)\right]^{\frac{1}{2}} \left(\frac{g\mu_B}{\beta k_B T}\right)$, A_1 represents a constant for the spin dependent scattering contribution to MR(H), J_{ex} is the s–d exchange integral. $D(E_F)$ is the density of state at Fermi level, S represents the spin of the localized magnetic moment, M^2 is the average of the squared magnetization, g is the Lande g-factor, k_B is the Boltzmann constant, μ_B is the Bohr magneton and T is the temperature. The coefficients c^2 and d^2 are given by, $c^2 = \frac{\sigma_1\sigma_2(\mu_1+\mu_2)^2}{(\sigma_1+\sigma_2)^2}$ and $d^2 = \frac{(\sigma_1\mu_2 - \sigma_2\mu_1)^2}{(\sigma_1+\sigma_2)^2}$, where σ_i and μ_i represent the conductivity and mobility of i^{th} carrier channel, respectively. This modified model accounts for the positive MR behavior observed in the samples at high temperatures, which is influenced by contributions from two-carrier conduction channels, while the negative MR dominates at low temperatures.

The resulting fits for Fe_3O_4 (7 nm)/MnP/Si are shown in Fig. 7(a–d), with fitting parameters (a, b, c and d) for both Fe_3O_4 (7 nm)/MnP/Si and MnP/Si listed in Table S2. A notable deviation from the experimental data is observed at higher fields (>|3| T) at ~65 K for Fe_3O_4 (7 nm)/MnP/Si (Fig. 7d) compared to MnP/Si (Fig. S10), suggesting the presence of an additional scattering mechanism, beyond the spin-dependent and impurity band scattering typically explained by the KF model. Below ~65 K, the MR data of the Fe_3O_4 (7 nm)/MnP

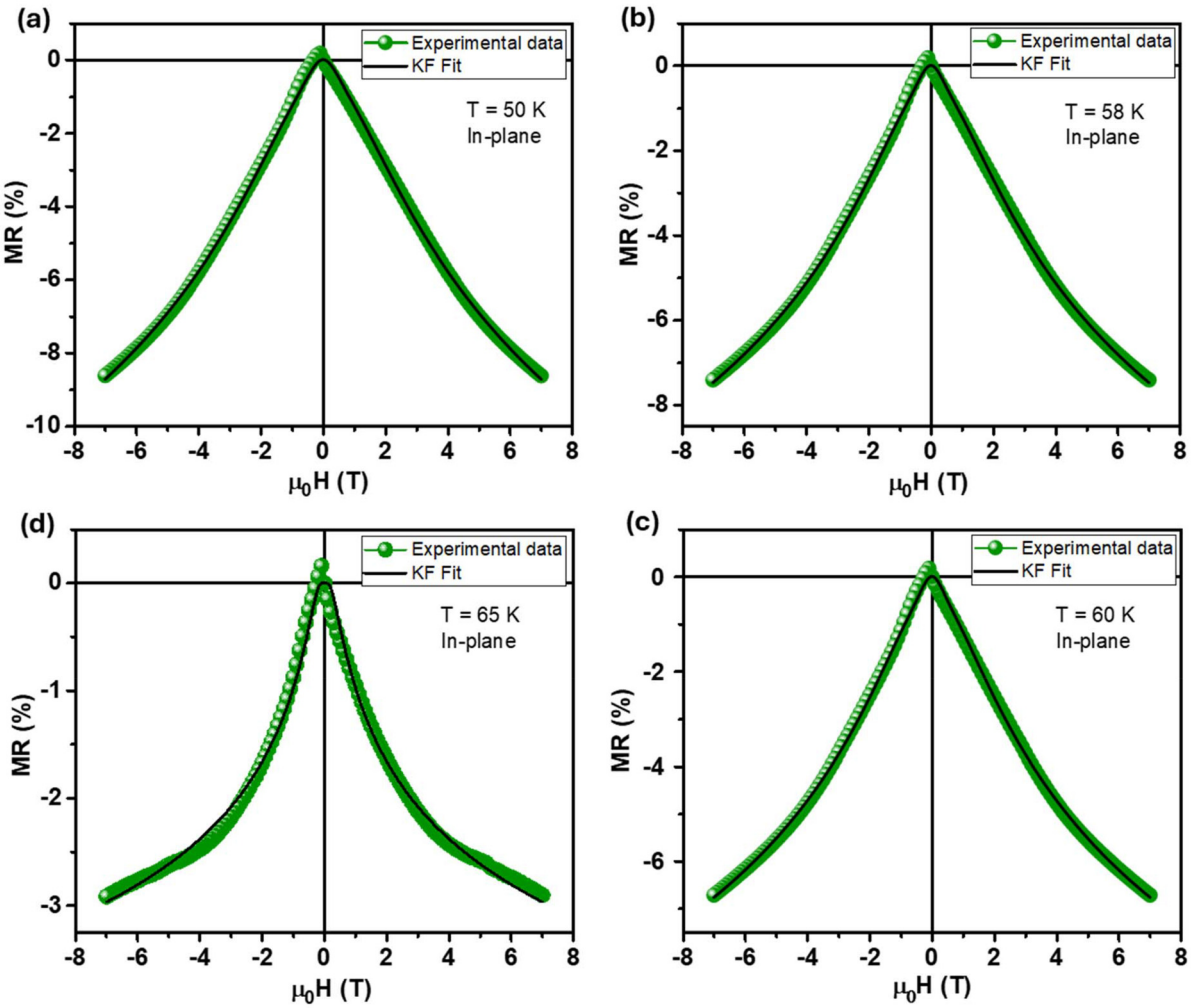

Fig. 7 In-plane (IP) magnetic field-dependent longitudinal magnetoresistance (MR) for Fe_3O_4 (7 nm)/MnP/Si at (a) 50 K, (b) 58 K, (c) 60 K, and (d) 65 K. The solid (red) lines represent the fitting curves using the equation of Khosla and Fischer (two band) model.

bilayer, like for the bare MnP film, agrees well with the KF model, indicating that the conventional scattering mechanisms dominate at low temperatures. Interestingly, the OP MR profile of Fe_3O_4 (7 nm)/MnP/Si (Fig. S11a) at 65 K reveals additional peaks around ±5 T, which are absent in the IP MR of Fe_3O_4 (7 nm)/MnP/Si (Fig. 7d) and the OP MR of MnP/Si (Fig. S11b). This points to the presence of complex magnetic interactions at the Fe_3O_4/MnP interface, which warrants further investigation to fully understand the underlying processes that influence the MR behavior in these bilayers.

Conclusion

In summary, this study demonstrates the successful growth of Fe_3O_4/MnP bilayers using pulsed laser deposition on MnP/Si substrates, with detailed structural, morphological, and magnetic characterizations. XRD and Raman spectroscopy confirmed the crystalline phases and proper growth of Fe_3O_4 and MnP, with notable differences in lattice parameters and surface morphology between Fe_3O_4 films grown on MnP and Si substrates. The Fe_3O_4/MnP interface exhibited distinct magnetic properties compared to Fe_3O_4/Si, likely due to strain and interfacial effects, as reflected in the surface roughness, grain size distribution, and magnetic domain structure. Magnetic force microscopy revealed stronger magnetic interactions and higher stray fields in the Fe_3O_4/MnP bilayers compared to Fe_3O_4/Si films, with variations in $\Delta\phi_{RMS}$ indicating substrate-dependent growth mechanisms. Magnetometry measurements indicate that the Fe_3O_4 layer significantly influences the magnetic properties of the MnP substrate, especially at lower temperatures. A shift in the ferromagnetic to helimagnetic transition of MnP from ~102 K to ~90 K in the Fe_3O_4/MnP bilayers was observed, attributed to strain-induced effects caused by the structural changes of Fe_3O_4 during its Verwey transition. The presence of the 7 nm-thick Fe_3O_4 layer enhances the Fe_3O_4/MnP interface coupling, resulting in the enhanced coercivity and saturation magnetization in the Fe_3O_4 (7 nm)/MnP bilayer compared to the bare MnP film. This can be attributed to the dual magnetic proximity effect and the impact of the structural transformation during the Verwey transition. In contrast, the strong soft ferromagnetic signal of the 58 nm-thick Fe_3O_4 layer dominates the overall magnetism of the Fe_3O_4 (58 nm)/MnP bilayer.

Furthermore, the temperature-dependent resistivity of Fe_3O_4/MnP bilayers revealed modifications in resistivity profiles due to the bilayer structure. The resistivity peak of MnP shifted to lower temperatures in the bilayers, indicating interfacial effects and the influence of Fe_3O_4 Verwey transition on the electronic transport properties of MnP. The MR magnitude showed significant enhancement with the Fe_3O_4 deposition, with thicker Fe_3O_4 layers (58 nm) yielding a greater MR effect compared to thinner layers (7 nm), further supporting the impact of interfacial coupling on the transport and magneto-transport properties. Overall, the results highlight the critical role of substrate and interfacial effects in determining the magnetic and electronic properties of Fe_3O_4/MnP bilayers, providing valuable insights for spintronic device applications. While our transport measurements suggest that Fe_3O_4 deposition modifies the low-temperature electronic response of MnP, direct studies of the valence band structure at the Fe_3O_4/MnP interface are not yet available. Future experimental (*e.g.*, ARPES, XPS) and theoretical work could provide deeper insight into the electronic reconstruction at this interface and its role in the observed transport phenomena.

Experimental methods

This study utilized MnP nanostructured thin films grown on Si substrates (MnP/Si) at a substrate temperature of 500 °C using molecular beam epitaxy. The growth of MnP has been documented elsewhere.[34] The MnP films used in this work had an average grain size of ~86 nm (film thickness ~100 nm), which corresponds to the larger-grained films that in our previous study exhibited a maximum MR of ~40%, as opposed to the smaller-grained (~39 nm) films that showed ~90% MR.[36] These larger-grained MnP films are chosen here as the baseline to evaluate the enhancement achievable by Fe_3O_4 overlayer deposition.

The MnP film was chemically cleaned (30 min in acetone, 30 min in methanol and 30 min in DI water with sonication) prior to characterizations, magnetic and transport measurements. Fe_3O_4 films with thicknesses of 7 nm and 58 nm were deposited on chemically cleaned MnP (Fe_3O_4/MnP/Si), while Fe_3O_4 films with thicknesses of 10 nm and 62 nm were grown directly on Si (Fe_3O_4/Si) using the pulsed laser deposition (PLD) technique. For the ablation, a focused KrF excimer laser (248 nm) and a commercially available Fe_3O_4 target were employed. The substrate temperatures for both Si and MnP during growth were maintained at 350 °C, with the chamber pressure held at 2×10^{-5}–2.2×10^{-5} Torr. The laser fluence was set at 2 J cm^{-2}, and the target-to-substrate distance was kept at 6 cm during deposition, with a repetition rate of 6 Hz. After deposition, the films were cooled to room temperature at a rate of 2 °C min^{-1} under the same chamber conditions as during growth. The presence of the Fe_3O_4 phase in the films was verified using Raman spectroscopy. Crystallinity of the MnP/Si, Fe_3O_4/MnP/Si bilayers, and Fe_3O_4/Si was assessed through X-ray diffraction (XRD, RIGAKU SmartLab). The presence of elements (Fe, O, Mn and P) in Fe_3O_4/MnP bilayers were confirmed using energy dispersive spectroscopy (EDS, Hitachi SU-70). Morphological analysis was performed using scanning electron microscopy (SEM, JEOL JSM-6390LV), while topography and root-mean-square (RMS) roughness were determined by atomic force microscopy (AFM, Hitachi AFM5300E) at room temperature and under vacuum. Magnetic domain images of the MnP and Fe_3O_4/MnP bilayers were captured using magnetic force microscopy (MFM) under similar conditions. Magnetometry and resistivity measurements were conducted using vibrating sample magnetometry and DC resistivity options of a Quantum Design Physical Property Measurement

System. Temperature-dependent magnetization (M–T) was measured under three protocols: zero-field cooling (ZFC), field-cooled cooling (FCC), and field-cooled warming (FCW) across a temperature range of 10 K to 350 K under a 0.1 T magnetic field. Field-dependent magnetization (M–H) was assessed under magnetic fields of ±5 T within the same temperature range for the MnP and Fe_3O_4/MnP bilayers. Finally, temperature-dependent resistivity ($\rho(T)$) and magnetic field-dependent longitudinal and transverse resistivity (MR) measurements were performed using a standard four-probe configuration across a temperature range of 10 K to 350 K and under magnetic fields of +7 T to −7 T (unipolar sweep). In this configuration, the magnetic field (H) were applied either along the plane of the film (IP) or perpendicular to the plane of the film (OP).

Author contributions

Conceptualization, investigation, methodology, writing – original draft, and writing – review and editing, N. W. Y. A. Y. M; investigation and writing – review and editing, D. D., and A. C.; investigation and writing – review, Y. M. W., and E. O.; resources, writing – review and editing, A. T. D., H. R. G., X. J., and S. W.; conceptualization, funding acquisition, supervision, and writing – review and editing, M. H. P.

Conflicts of interest

The authors declare no conflicts of interest.

Data availability

The raw data required to reproduce the findings cannot be shared at this time as the data also forms part of an ongoing study.

Supplementary information (SI) is available. See DOI: https://doi.org/10.1039/d5nr02716k.

Acknowledgements

Research at USF was supported by the U.S. Department of Energy, Office of Basic Energy Sciences, Division of Materials Sciences and Engineering under award no. DE-FG02-07ER46438 (structural, magnetic and magneto-transport studies).

References

1 J. Kishine and A. S. Ovchinnikov, in *Solid State Physics*, ed. R. E. Camley and R. L. Stamps, Academic Press, 2015, vol. **66**, pp. 1–130.
2 D. Mandrus, in *Encyclopedia of Materials: Electronics*, Elsevier, 2023, vol. 1, p. 796.
3 Y. Tokura and N. Kanazawa, *Chem. Rev.*, 2021, **121**, 2857.
4 J. Müller, J. Rajeswari, P. Huang, Y. Murooka, H. M. Rønnow, F. Carbone and A. Rosch, *Phys. Rev. Lett.*, 2017, **119**, 137201.
5 X. Zhao, J. Tang, K. Pei, W. Wang, S.-Z. Lin, H. Du, M. Tian and R. Che, *Nano Lett.*, 2022, **22**, 8793.
6 Y. Cao, Z. Huang, Y. Yin, H. Xie, B. Liu, W. Wang, C. Zhu, D. Mandrus, L. Wang and W. Huang, *Mater. Today Adv.*, 2020, **7**, 100080.
7 H. Ishizuka and N. Nagaosa, *Sci. Adv.*, 2018, **4**, 29487909.
8 C. Zhang, J. Zhang, C. Liu, S. Zhang, Y. Yuan, P. Li, Y. Wen, Z. Jiang, B. Zhou, Y. Lei, D. Zheng, C. Song, Z. Hou, W. Mi, U. Schwingenschlögl, A. Manchon, Z. Q. Qiu, H. N. Alshareef, Y. Peng and X. Zhang, *Adv. Mater.*, 2021, **33**, 2101131.
9 G. Kimbell, C. Kim, W. Wu, M. Cuoco and J. W. A. Robinson, *Commun. Mater.*, 2022, **3**, 19.
10 S.-W. Cheong and F.-T. Huang, *Appl. Phys. Lett.*, 2024, **125**, 060501.
11 P. Behera, M. A. May, F. Gómez-Ortiz, S. Susarla, S. Das, C. T. Nelson, L. Caretta, S.-L. Hsu, M. R. McCarter, B. H. Savitzky, E. S. Barnard, A. Raja, Z. Hong, P. García-Fernandez, S. W. Lovesey, G. van der Laan, P. Ercius, C. Ophus, L. W. Martin, J. Junquera, M. B. Raschke and R. Ramesh, *Sci. Adv.*, 2022, **8**, 34985953.
12 V. V. Ustinov and I. A. Yasyulevich, *Phys. Rev. B*, 2022, **106**, 064417.
13 N. Jiang, Y. Nii, H. Arisawa, E. Saitoh and Y. Onose, *Nat. Commun.*, 2020, **11**, 1601.
14 H. Masuda, T. Seki, J. Ohe, Y. Nii, H. Masuda, K. Takanashi and Y. Onose, *Nat. Commun.*, 2024, **15**, 1999.
15 I. Ennen, D. Kappe, T. Rempel, C. Glenske and A. Hütten, *Sensors*, 2016, **16**, 904.
16 D. J. Campbell, J. Collini, J. Sławińska, C. Autieri, L. Wang, K. Wang, B. Wilfong, Y. S. Eo, P. Neves, D. Graf, E. E. Rodriguez, N. P. Butch, M. Buongiorno Nardelli and J. Paglione, *npj Quantum Mater.*, 2021, **6**, 38.
17 F. Li, H. Nie, Y. Zhao, Z. Zhao, J. Huo, T. Wang, Z. Liao, A. Liu, H. Guo, H. Shen, S. Jiang, R. Chen, A. Yan, S.-W. Cheong, W. Xia, J. Sun and L. Zhang, *Appl. Phys. Rev.*, 2024, **11**, 021423.
18 S. Banik, M. K. Chattopadhyay, S. Tripathi, R. Rawat and S. N. Jha, *Sci. Rep.*, 2020, **10**, 12030.
19 A. Zadorozhnyi, R. Rivlis and Y. Dahnovsky, *Phys. Rev. B*, 2023, **108**, 014405.
20 S. M. Stishov and A. E. Petrova, *Phys.-Usp.*, 2011, **54**, 1117.
21 M. S. Reis, R. M. Rubinger, N. A. Sobolev, M. A. Valente, K. Yamada, K. Sato, Y. Todate, A. Bouravleuv, P. J. von Ranke and S. Gama, *Phys. Rev. B: Condens. Matter Mater. Phys.*, 2008, **77**, 104439.
22 R. P. Madhogaria, C.-M. Hung, B. Muchharla, A. T. Duong, R. Das, P. T. Huy, S. Cho, S. Witanachchi, H. Srikanth and M.-H. Phan, *Phys. Rev. B*, 2021, **103**, 184423.
23 N. Martin, I. Mirebeau, C. Franz, G. Chaboussant, L. N. Fomicheva and A. V. Tsvyashchenko, *Phys. Rev. B*, 2019, **99**, 100402.

24 S. Akatsuka, S. Esser, S. Okumura, R. Yambe, R. Yamada, M. M. Hirschmann, S. Aji, J. S. White, S. Gao, Y. Onuki, T. Arima, T. Nakajima and M. Hirschberger, *Nat. Commun.*, 2024, **15**, 4291.
25 J. A. Schneeloch, S. Liu, P. V. Balachandran, Q. Zhang and D. Louca, *Phys. Rev. B*, 2024, **109**, 144403.
26 E. M. Clements, R. Das, M.-H. Phan, L. Li, V. Keppens, D. Mandrus, M. Osofsky and H. Srikanth, *Phys. Rev. B*, 2018, **97**, 214438.
27 E. M. Clements, R. Das, L. Li, P. J. Lampen-Kelley, M.-H. Phan, V. Keppens, D. Mandrus and H. Srikanth, *Sci. Rep.*, 2017, **7**, 6545.
28 T. Miyadai, K. Kikuchi, H. Kondo, S. Sakka, M. Arai and Y. Ishikawa, *J. Phys. Soc. Jpn.*, 1983, **52**, 1394.
29 H. Watanabe, Y. Tazuke and H. Nakajima, *J. Phys. Soc. Jpn.*, 1985, **54**, 3978.
30 S. L. Zhang, I. Stasinopoulos, T. Lancaster, F. Xiao, A. Bauer, F. Rucker, A. A. Baker, A. I. Figueroa, Z. Salman, F. L. Pratt, S. J. Blundell, T. Prokscha, A. Suter, J. Waizner, M. Garst, D. Grundler, G. van der Laan, C. Pfleiderer and T. Hesjedal, *Sci. Rep.*, 2017, **7**, 123.
31 S. E. Dissanayake, M. Matsuda, K. Yoshimi, S. Kasamatsu, F. Ye, S. Chi, W. Steinhardt, G. Fabbris, S. Haravifard, J. Cheng, J. Yan, J. Gouchi and Y. Uwatoko, *Phys. Rev. Res.*, 2023, **5**, 043026.
32 X. Sun, S. Zhao, A. Bachmatiuk, M. H. Rümmeli, S. Gorantla, M. Zeng and L. Fu, *Small*, 2020, **16**, 2001484.
33 C.-M. Hung, R. P. Madhogaria, B. Muchharla, E. M. Clements, A. T. Duong, R. Das, P. T. Huy, S. Cho, S. Witanachchi, H. Srikanth and M.-H. Phan, *Phys. Status Solidi A*, 2022, **219**, 2100367.
34 A.-T. Duong, T. M. H. Nguyen, D.-L. Nguyen, R. Das, H.-T. Nguyen, B. T. Phan and S. Cho, *J. Magn. Magn. Mater.*, 2019, **482**, 287.
35 A. De Andrés, R. Ramrez-Jiménez, M. García-Hernández, S. Lambert-Milot and R. A. Masut, *Appl. Phys. Lett.*, 2011, **99**, 182506.
36 N. W. Y. A. Y. Mudiyanselage, D. DeTellem, A. Chanda, A. T. Duong, T.-E. Hsieh, J. Frisch, M. Bär, R. P. Madhogaria, S. Mozaffari, H. S. Arachchige, D. Mandrus, H. Srikanth, S. Witanachchi and M.-H. Phan, *ACS Appl. Mater. Interfaces*, 2025, **17**, 25429–25441.
37 X. Wang, Y. Liao, D. Zhang, T. Wen and Z. Zhong, *J. Mater. Sci. Technol.*, 2018, **34**, 1259.
38 X. W. Li, A. Gupta, G. Xiao and G. Q. Gong, *J. Appl. Phys.*, 1998, **83**, 7049.
39 M. D. Nguyen, H.-V. Tran, S. Xu and T. R. Lee, *Appl. Sci.*, 2021, **11**, 11301.
40 P. Li, C. Jin, W.-B. Mi and H.-L. Bai, *Chin. Phys. B*, 2013, **22**, 047505.
41 X. H. Liu, A. D. Rata, C. F. Chang, A. C. Komarek and L. H. Tjeng, *Phys. Rev. B: Condens. Matter Mater. Phys.*, 2014, **90**, 125142.
42 S. Mishra, K. Dey, U. Chowdhury, D. Bhattacharya, C. K. Ghosh and S. Giri, *AIP Adv.*, 2017, **7**, 125015.
43 W. B. Mi, E. Y. Jiang and H. L. Bai, *J. Appl. Phys.*, 2010, **107**, 103922.
44 F. Greullet, E. Snoeck, C. Tiusan, M. Hehn, D. Lacour, O. Lenoble, C. Magen and L. Calmels, *Appl. Phys. Lett.*, 2008, **92**, 053508.
45 C.-M. Hung, D. T.-X. Dang, A. Chanda, D. Detellem, N. Alzahrani, N. Kapuruge, Y. T. H. Pham, M. Liu, D. Zhou, H. R. Gutierrez, D. A. Arena, M. Terrones, S. Witanachchi, L. M. Woods, H. Srikanth and M.-H. Phan, *Nanomaterials*, 2023, **13**, 771.
46 A. Chanda, C.-M. Hung, A. T. Duong, S. Cho, H. Srikanth and M.-H. Phan, *J. Magn. Magn. Mater.*, 2023, **568**, 170370.
47 A. Chanda, D. Detellem, Y. T. H. Pham, J. E. Shoup, A. T. Duong, R. Das, S. Cho, D. V. Voronine, M. T. Trinh, D. A. Arena, S. Witanachchi, H. Srikanth and M. H. Phan, *ACS Appl. Mater. Interfaces*, 2022, **14**, 13468.
48 V. E. Sergeev, V. M. Vorotyntsev, T. S. Sazanova, I. V. Vorotyntsev and S. V. Kononov, *J. Surf. Invest.: X-Ray, Synchrotron Neutron Tech.*, 2020, **14**, 875.
49 F. Lan, R. Zhou, Z. Qian, Y. Chen and L. Xie, *Crystals*, 2022, **12**, 485.
50 P. Kumar, H. No-Lee and R. Kumar, *J. Mater. Sci.: Mater. Electron.*, 2014, **25**, 4553.
51 S. Tiwari, D. M. Phase and R. J. Choudhary, *Appl. Phys. Lett.*, 2008, **93**, 234108.
52 Z. Luo, Y. Lu, D. W. Singer, M. E. Berck, L. A. Somers, B. R. Goldsmith and A. T. C. Johnson, *Chem. Mater.*, 2011, **23**, 1441.
53 A. Bollero, M. Ziese, R. Höhne, H. C. Semmelhack, U. Köhler, A. Setzer and P. Esquinazi, *J. Magn. Magn. Mater.*, 2005, **285**, 279.
54 A. D. Wei, J. R. Sun, Y. Z. Chen, W. M. Lü and B. G. Shen, *J. Phys. D: Appl. Phys.*, 2010, **43**, 205004.
55 L. Yue and S.-H. Liou, in *Scanning Probe Microscopy in Nanoscience and Nanotechnology*, ed. B. Bharat, Springer, Berlin, Heidelberg, 2011, vol. 2, pp. 287–319.
56 O. Kazakova, R. Puttock, C. Barton, H. Corte-León, M. Jaafar, V. Neu and A. Asenjo, *J. Appl. Phys.*, 2019, **125**, 060901.
57 A. Chanda, D. Rani, D. DeTellem, N. Alzahrani, D. A. Arena, S. Witanachchi, R. Chatterjee, M. H. Phan and H. Srikanth, *ACS Appl. Mater. Interfaces*, 2023, **15**, 53697.
58 Y. Jin, L. Yue and D. J. Sellmyer, *Thin Solid Films*, 2017, **636**, 283.
59 J. Hu, J. Luo, Y. Zheng, J. Chen, G. J. Omar, A. T. S. Wee and A. Ariando, *J. Alloys Compd.*, 2022, **911**, 164830.
60 H. Palonen, F. Magnus and B. Hjörvarsson, *Phys. Rev. B*, 2018, **98**, 144419.
61 P. K. Manna and S. M. Yusuf, *Phys. Rep.*, 2014, **535**, 61.
62 J. Choi, S. Choi, M. H. Sohn, H. Park, Y. Park, H.-M. Park, S. C. Hong and S. Cho, *J. Magn. Magn. Mater.*, 2006, **304**, e112.
63 A. De Andrés, A. Espinosa, C. Prieto, M. Garca-Hernndez, R. Ramrez-Jiménez, S. Lambert-Milot and R. A. Masut, *J. Appl. Phys.*, 2011, **109**, 113910.

64 K. A. Gregg, S. C. Perera, G. Lawes, S. Shinozaki and S. L. Brock, *Chem. Mater.*, 2006, **18**, 879.
65 E. Hirahara, T. Suzuki and Y. Matsumura, *J. Appl. Phys.*, 1968, **39**, 713.
66 X. Guan, R. Ma, G. Zhou, Z. Quan, G. A. Gehring and X. Xu, *J. Mater. Sci.*, 2020, **55**, 99.
67 H. Takahashi, S. Soeya, J. Hayakawa, K. Ito, A. Kida, C. Yamamoto, H. Asano and M. Matsui, *J. Appl. Phys.*, 2003, **93**, 8029.
68 A. Chanda, C. Holzmann, N. Schulz, J. Seyd, M. Albrecht, M. Phan and H. Srikanth, *Adv. Funct. Mater.*, 2022, **32**, 2109170.
69 H. T. Wu, T. Min, Z. X. Guo and X. R. Wang, *Front. Phys.*, 2022, **10**, 1068605.
70 R. Gunnarsson, Z. G. Ivanov, C. Dubourdieu and H. Roussel, *Phys. Rev. B: Condens. Matter Mater. Phys.*, 2004, **69**, 054413.
71 R. K. Dumas, P. K. Greene, D. A. Gilbert, L. Ye, C. Zha, J. Åkerman and K. Liu, *Phys. Rev. B: Condens. Matter Mater. Phys.*, 2014, **90**, 104410.
72 S. Zhang and P. M. Levy, *J. Appl. Phys.*, 1993, **73**, 5315.
73 W. Wang, F. Zhu, W. Lai, J. Wang, G. Yang, J. Zhu and Z. Zhang, *J. Phys. D: Appl. Phys.*, 1999, **32**, 1990.
74 R. P. Khosla and J. R. Fischer, *Phys. Rev. B*, 1970, **2**, 4084.